◆ Human Brain Mapping 38:3704–3722 (2017) ◆

Gray Matter Abnormalities in Idiopathic Parkinson's Disease: Evaluation by Diffusional Kurtosis Imaging and Neurite Orientation Dispersion and Density Imaging

Koji Kamagata,[1,2]* Andrew Zalesky,[2,3] Taku Hatano,[4] Ryo Ueda,[5] Maria Angelique Di Biase,[2] Ayami Okuzumi,[4] Keigo Shimoji,[6] Masaaki Hori,[1] Karen Caeyenberghs,[7] Christos Pantelis,[2,3,8] Nobutaka Hattori,[4] and Shigeki Aoki[1]

[1]*Department of Radiology, Juntendo University Graduate School of Medicine, Tokyo, Japan*
[2]*Melbourne Neuropsychiatry Centre, Department of Psychiatry, The University of Melbourne & Melbourne Health, Parkville, VIC, Australia*
[3]*Melbourne School of Engineering, University of Melbourne, Melbourne, Australia*
[4]*Department of Neurology, Juntendo University Graduate School of Medicine, Tokyo, Japan*
[5]*Department of Radiological Sciences, Graduate School of Human Health Sciences, Tokyo Metropolitan University, Tokyo, Japan*
[6]*Department of Diagnostic Radiology, Tokyo Metropolitan Geriatric Hospital, Tokyo, Japan*
[7]*School of Psychology, Faculty of Health Sciences, Australian Catholic University, Fitzroy, VIC, Australia*
[8]*Centre for Neural Engineering, Department of Electrical and Electronic Engineering, The University of Melbourne, Carlton, VIC, Australia*

Abstract: Mapping gray matter (GM) pathology in Parkinson's disease (PD) with conventional MRI is challenging, and the need for more sensitive brain imaging techniques is essential to facilitate early diagnosis and assessment of disease severity. GM microstructure was assessed with GM-based spatial statistics applied to diffusion kurtosis imaging (DKI) and neurite orientation dispersion imaging (NODDI) in 30 participants with PD and 28 age- and gender-matched controls. These were compared with currently used assessment methods such as diffusion tensor imaging (DTI), voxel-based morphometry (VBM), and surface-based cortical thickness analysis. Linear discriminant analysis (LDA) was also used to test whether subject diagnosis could be predicted based on a linear combination of regional diffusion metrics. Significant differences in GM microstructure were observed in the striatum and the frontal, temporal, limbic, and paralimbic areas in PD patients using DKI and NODDI. Significant correlations between motor deficits and GM microstructure were also noted in these areas. Traditional VBM and surface-based cortical thickness analyses failed to detect any GM differences. LDA

Additional Supporting Information may be found in the online version of this article.

We declare that we have no conflicts of interest.

Contract grant sponsor: Hitachi, Ltd.; Contract grant sponsor: the program for Brain Mapping by Integrated Neurotechnologies for Disease Studies (Brain/MINDS) from the Japan Agency for Medical Research and Development (AMED); Contract grant sponsor: JSPS KAKENHI; Contract grant number: JP16K19854

*Correspondence to: Koji Kamagata, MD, PhD; Department of Radiology, Juntendo University School of Medicine, 2-1-1 Hongo, Bunkyo-ku, Tokyo 113-8421, Japan. E-mail: kkamagat@juntendo.ac.jp

Received for publication 1 December 2016; Revised 22 February 2017; Accepted 17 April 2017.

DOI: 10.1002/hbm.23628

Published online 4 May 2017 in Wiley Online Library (wileyonlinelibrary.com).

indicated that mean kurtosis (MK) and intra cellular volume fraction (ICVF) were the most accurate predictors of diagnostic status. In conclusion, DKI and NODDI can detect cerebral GM abnormalities in PD in a more sensitive manner when compared with conventional methods. Hence, these methods may be useful for the diagnosis of PD and assessment of motor deficits. *Hum Brain Mapp 38:3704–3722, 2017.*

Key words: diffusion MRI; diffusion tensor imaging; discriminant analysis; Lewy bodies; limbic system; neurodegenerative disorders

INTRODUCTION

Parkinson's disease (PD) is neuropathologically characterized by the presence of degenerating nigrostriatal dopaminergic neurons in the substantia nigra, and Lewy neurites (LNs) as well as Lewy bodies (LBs), the main components of the Lewy-related pathology in the brain [Braak and Del Tredici, 2008]. LB formation is considered a pathological hallmark of degenerating neurons in patients with PD, which involves widespread progression throughout the cortex. According to the established staging model of PD proposed by Braak et al., Lewy-type pathology initially involves the medulla oblongata and olfactory bulb (Braak stage I, II), followed by the limbic areas (Braak stage III) and the anteromedial temporal and paralimbic cortices, as well as the thalamus (Braak stage IV). With disease progression, pathology extends to the striatal, insular and associated areas of neocortex (Braak stage V), and finally reaches the primary sensory/motor fields of the neocortex (Braak stage VI) [Braak and Del Tredici, 2008]. The onset of PD-related motor symptoms is thought to occur during Braak stages III and IV [Braak and Del Tredici, 2008].

The severity of parkinsonian motor deficits is primarily due to neuronal loss in the substantia nigra and the consequent loss of striatal dopaminergic terminals [Greffard et al., 2006]. Meanwhile, cortical pathology is closely related to cognitive impairment and other non-motor symptoms in PD [Apaydin et al., 2002; Braak et al., 2005]. However, a postmortem study showed that disease duration and motor severity were correlated with Braak stages in PD [Braak et al., 2005]. In another postmortem study, the response to anti-parkinsonian therapy was found to decline in cases where the Lewy-related pathology had spread throughout the cerebral cortex and limbic system [Apaydin et al., 2002]. It is known that the clinical motor deficit response to levodopa treatment worsens as PD progresses [Bonnet et al., 1987], and cortex pathology is considered to reflect the progression of PD. Given the well-characterized temporal changes in the cortex, markers of cortical pathology appear to be useful in establishing a PD diagnosis and evaluating its severity.

To examine the pathology of the cortical and subcortical structures *in vivo* in patients with PD, many studies have employed morphological MRI techniques such as, voxel based morphometry (VBM) [Ashburner and Friston, 2000] and surface based cortical thickness analysis [Fischl and Dale, 2000], which measure brain volume and cerebral cortical thickness, respectively. However, these methods have produced inconsistent results. Several studies have reported no significant changes in cortical morphology in PD patients with normal cognitive function [Cerasa et al., 2011; Feldmann et al., 2008; Messina et al., 2011; Paviour et al., 2006; Rizzo et al., 2008; Seppi and Poewe, 2010]. On the contrary, there are many reports on the occurrence of widespread atrophy in the frontal, temporal, limbic, and paralimbic areas of the brain [Biundo et al., 2011; Burton et al., 2004; Jubault et al., 2011; Lyoo et al., 2010; Meppelink et al., 2011; Tinaz et al., 2011]. These differences in findings may be attributed to the different MRI acquisition and processing techniques used, as well as the variability in disease stage; nevertheless, these inconsistencies can result from mild or subtle brain atrophy in PD patients with normal cognitive function, which may remain undetected following the use of conventional gray matter (GM) analysis methods.

Many studies have utilized diffusion tensor imaging (DTI) in order to detect in vivo changes in intracerebral microstructures caused by PD [Chan et al., 2007; Gattellaro et al., 2009; Kamagata et al., 2012; Kamagata et al., 2013; Karagulle Kendi et al., 2008; Zhan et al., 2012]. DTI can resolve the micron-scale displacement of water molecules that diffuse into the tissue, and may be used to evaluate neural tissue microstructure *in vivo*. Studies using DTI in PD have reported a decrease in fractional anisotropy (FA) in the substantia nigra and corpus striatum. [Chan et al., 2007; Vaillancourt et al., 2009; Yoshikawa et al., 2004; Zhan et al., 2012]. Moreover, the extent of reduction in FA has been associated with the severity of the clinical symptoms [Chan et al., 2007; Zhan et al., 2012]. Other studies have reported no significant differences in DTI parameters measured in the striatum [Chan et al., 2007; Cochrane and Ebmeier, 2013; Nicoletti et al., 2013; Paviour et al., 2006; Zhan et al., 2012]. Significantly lower FA in the white matter (WM) of the frontal lobes, such as the motor, premotor, and supplementary prefrontal areas, has also been reported [Gattellaro et al., 2009; Karagulle Kendi et al., 2008; Yoshikawa et al., 2004; Zhan et al., 2012] as well as in the white matter of the limbic system, such as the anterior cingulate [Kamagata et al., 2012; Karagulle Kendi

et al., 2008]. DTI assumes that water diffusion has a Gaussian probability distribution in biological tissue [Basser and Jones, 2002]. However, water in biological tissue often displays non-Gaussian diffusion because it is restricted by diffusion barriers such as, cell membranes and organelles. Therefore, the assumption of Gaussian water diffusion may be inappropriate in biological tissue. Moreover, DTI cannot thoroughly describe microstructural changes in GM because water diffusion is relatively isotropic [Lu et al., 2006]. For these reasons, DTI is not used in the assessment of gray matter regions (especially the cortex) other than the substantia nigra and striatum in patients with PD. Several studies have reported the absence of significant differences between PD and healthy groups following the use of DTI to assess the substantia nigra [Focke et al., 2011; Menke et al., 2009]; on the other hand there are reports of FA increase in patients with PD [Wang et al., 2011], therefore, leading to a lack of consensus regarding the use of DTI in these patients.

To improve the sensitivity of MRI in detecting subtle pathologies in PD, we propose the use of multishell diffusion MRI (dMRI) modalities, including diffusional kurtosis imaging (DKI) [Jensen et al., 2005] and neurite orientation dispersion and density imaging (NODDI) [Zhang et al., 2012]. DKI has been proposed as a means of quantifying non-Gaussian water diffusion [Fieremans et al., 2011; Jensen and Helpern, 2010; Jensen et al., 2005; Veraart et al., 2011]. In contrast to conventional DTI, DKI is not limited to anisotropic environments such as WM; hence, it especially permits the quantification of the microstructural integrity of GM [Jensen et al., 2005]. In addition, NODDI-derived metrics capture the density and direction of neurites (axons and dendrites) by assuming a three-compartment (intracellular, extracellular, and cerebrospinal fluid) biophysical tissue model for each voxel. Therefore, NODDI provides specific information regarding pathological processes in the cortex when compared with traditional DTI metrics [Zhang et al., 2012].

The use of DKI and NODDI has been reported in previous studies investigating the basal ganglia and substantia nigra pars compacta (SNpc) [Kamagata et al., 2015; Surova et al., 2016;Wang et al., 2011]. However, these studies used manually traced regions of interest and did not evaluate the cerebral cortex. In the present study, we aimed to assess the ability of DKI and NODDI to detect Lewy-related pathology across the entire cortex and subcortical structures in PD patients. We hypothesized that whole-brain DKI and NODDI offer increased sensitivity and specificity in the detection of subtle Lewy-related cortical pathology in PD when compared with the measures derived from conventional DTI, VBM and surface-based cortical thickness. To test this hypothesis, we compared results obtained from dMRI modalities (DKI, NODDI, and conventional DTI), with GM volumes derived from VBM and surface-based cortical thickness measures.

MATERIALS AND METHODS

Subjects

This study was approved by an institutional review board. Informed consent was obtained from all participants before evaluation. A total of 30 patients with PD, recruited between August 2015 and April 2016, participated in this study. All 30 patients were diagnosed by movement disorder specialists and met the *United Kingdom Parkinson's Disease Society Brain Bank* criteria [Hughes et al., 1992]. Disease severity was assessed using the motor scores of the *Unified Idiopathic Parkinson's Disease Rating Scale* (UPDRS)-III [Martinez-Martin et al., 1994], as well as the Hoehn and Yahr staging scale [Hoehn and Yahr, 1967]. All patients were taking levodopa in combination with a dopamine decarboxylase inhibitor (beneserazide or carbidopa) at the time of MRI and clinical examinations. Eighteen months or more post diagnosis, all patients remained free of Atypical Parkinsonism and continued to respond to antiparkinsonian therapy. Twenty-eight age- and gender-matched healthy controls with no history of neuropsychiatric diseases were recruited into the study. None of the control subjects showed abnormal signals in structural MRI. The demographic and clinical characteristics of all participants are shown in Table I.

Magnetic Resonance Imaging (MRI) Acquisition

All MR images were obtained on a 3.0-T system (Achieva; Philips Healthcare, Best, The Netherlands). A spin-echo echo-planar imaging diffusion-weighted scheme was obtained consisting of two *b*-values (1,000 and 2,000 s/mm^2) acquired along 32 uniformly distributed directions in an anterior-posterior phase encoding direction. Each diffusion-weighted acquisition was complemented with a gradient-free image ($b = 0$). Standard and reverse phase encoded blipped image with no diffusion weighting (Blip Up and Blip Down) were also acquired to correct for magnetic susceptibility-induced distortions related to the EPI acquisitions [Andersson, et al., 2016]. The sequence parameters were as follows: repetition time, 9,810 ms; echo time, 100 ms; diffusion gradient pulse duration (δ), 21.4 ms; diffusion gradient separation (Δ), 39.6 ms; field of view (FOV), 256 × 256 mm; matrix size, 128 × 128; slice thickness, 2 mm; and acquisition time, 13.07 min. The MRI parameters of the three-dimensional MP-RAGE were as follows: repetition time, 15 ms; echo time, 3.54 ms; inversion time, 1,100 ms; thickness, 0.86 mm; FOV, 22 × 22 mm; matrix size, 256 × 256, and acquisition time, 5.14 min.

Diffusion Metric Analysis (DKI, NODDI, Conventional DTI)

Pre-processing diffusion data

All datasets were checked visually in all three orthogonal views, none of which was found to exhibit severe

TABLE I. Demographic characteristics of subjects

	NC (n = 28)	All PD patients (n = 30)	Left sided onset PD (n = 17)	Right sided onset PD (n =11)	χ^2 or t value/ P value (NC vs. all PD)	χ^2 or t value/ P value (Left onset PD vs. Right onset PD)	χ^2 or t value/ P value (NC vs. Left onset PD)	χ^2 or t value/P value (NC vs. Right onset PD)
Sex, male:female	10:18	12:18	8:9	3:8	0.11/0.74	1.09/0.30	0.56/0.45	0.32/0.57
Age in years, mean (SD), Range	66.5 (10.8) 46–83	67.6 (9.8) 44–80	69.2 (7.4) 58–79	66.1 (11.0) 44–80	−0.42/0.68	−0.86/0.40	−0.90/0.37	0.10/0.93
Side onset L/R/B	0	11/17/2	11/0/0	0/17/0	–	–	–	–
Disease duration in years, mean (SD)	0	6.4 (3.7)	6.6 (3.1)	5.5 (3.7)	–	−0.83/0.42	–	–
Hoehn–Yahr stage (SD)	0	2.1 (0.9)	1.9 (0.7)	2.0 (0.6)	–	0.22/0.83	–	–
UPDRS III-motor subscale score, median (SD)	0	16.1 (8.8)	16.1 (8.6)	15.9 (9.0)	–	−0.06/0.95	–	–
Neuroimaging data								
Total gray matter volume (mL)	561.86 (48.65)	563.57 (52.81)	550.62 (51.65)	586.58 (57.21)	−0.13/0.90	1.74/0.09	0.74/0.46	−1.32/0.20
Total white matter volume (mL)	428.13 (51.78)	449.40 (62.36)	438.39 (65.65)	462.56 (56.90)	−1.38/0.17	1.34/0.19	−0.59/0.56	−1.77/0.09
Intracranial volume (mL)	1,265.31 (249.19)	1,326.04 (251.58)	1,310.85 (249.52)	1,332.43 (240.80)	−0.91/0.37	0.23/0.82	−0.60/0.55	−0.66/0.51

L/R/B, left/right/both; UPDRS, Unified Idiopathic Parkinson's Disease Rating Scale; PD, Parkinson disease; NS, not significant; SD, standard deviation; NA, not applicable; NC, normal controls.

TABLE II. Summary of diffusion MRI models and derived parameters used in the present study.

Diffusion MRI model	Parameter	Abbreviations	Parameters related to
Diffusion tensor imaging	FA	Fractional anisotropy	overall directionality of water diffusion within brain tissue
	MD	Mean diffusivity	magnitude of isotropic diffusion within brain tissue
	AD	Axial diffusivity	magnitude of isotropic diffusion within brain tissue along the direction of maximal diffusion
	RD	Radial diffusivity	magnitude of isotropic diffusion within brain tissue perpendicular to direction of maximal diffusion
Diffusional kurtosis imaging	MK	Mean kurtosis	microstructural complexity or heterogeneity within brain tissue
	AK	Axial kurtosis	microstructural complexity or heterogeneity within brain tissue along the direction of maximal diffusion
	RK	Radial kurtosis	microstructural complexity or heterogeneity within brain tissue perpendicular to direction of maximal diffusion
Neurite orientation dispersion and density imaging	ICVF	Intracellular volume fraction	density of neurites (axons and dendrites) based on intracellular diffusion
	OD	Orientation dispersion index	dispersion of neurites (axons and dendrites) in the intracellular compartment
	ISOVF	Isotropic volume fraction	volume fraction of isotropic diffusion

artifacts (e.g., gross geometric distortion, signal dropout, bulk motion). The diffusion-weighted data were corrected for susceptibility-induced geometric distortions, eddy current distortions, and inter-volume subject motion using EDDY and TOPUP toolboxes [Andersson and Sotiropoulos, 2016].

Diffusion metrics

The resulting images were fitted to the NODDI model [Zhang et al., 2012] using the NODDI Matlab Toolbox5 (http://www.nitrc.org/projects/noddi_toolbox) and *Accelerated Microstructure Imaging via Convex Optimization* (AMICO) [Daducci et al., 2015]. Maps of intracellular volume fraction (ICVF), orientation dispersion index (OD), and isotropic volume fraction (ISOVF) were generated.

To estimate the heterogeneity or complexity of the tissue microstructure, the diffusion-weighted data were also processed using the Diffusional Kurtosis Estimator [Tabesh et al., 2011] implemented in MATLAB (Math-Works, Natick, MA). Voxel-wise maps were generated for mean kurtosis (MK), axial kurtosis (AK), and radial kurtosis (RK).

The classic diffusion tensor was estimated using ordinary least squares applied to the diffusion-weighted images with $b = 0$ and 1,000 s/mm^2. Once the diffusion tensor was estimated, FA, MD, axial diffusivity (AD), and radial diffusivity (RD) were then estimated based on standard formulae [Basser, et al., 1994]. The parameters of DTI, DKI, and NODDI are summarized in Table II. A mask was applied comprising all brain voxels with an ISOVF below 90% to all diffusion parameter maps in order to exclude the CSF component.

Diffusion Metric Voxel-Wise Analysis

GM-based spatial statistics (GBSS) [Ball et al., 2013; Nazeri et al., 2015] were used to regionally map significant patient-control differences in each of the NODDI, DKI and DTI metrics (10 metrics in total). The partial volume effect (PVE) of WM and cerebrospinal fluid (CSF) proximal to the cortex can lead to errors while measuring the dMRI parameters of the cerebral cortex; therefore, we used GBSS [Ball et al., 2013] to exclude the effects of WM and CSF PVE. This method is a GM analogue of tract-based spatial statistics (TBSS) [Smith et al., 2006] and ensures accurate anatomical alignment between subjects with the use of a skeleton projection step. Classic registration methods can present difficulty in normalizing an individual's brain anatomy to a common template, particularly in the presence of pathology. associated with regional morphological changes. We used GBSS to reduce the effects of any residual spatial misalignment between individuals that may have resulted from the complex cortical geometry and pathology. By creating a skeleton of the cerebral cortex and consolidating parameters of the surrounding regions into those of the skeleton, it is possible to avoid PVE of WM and CSF.

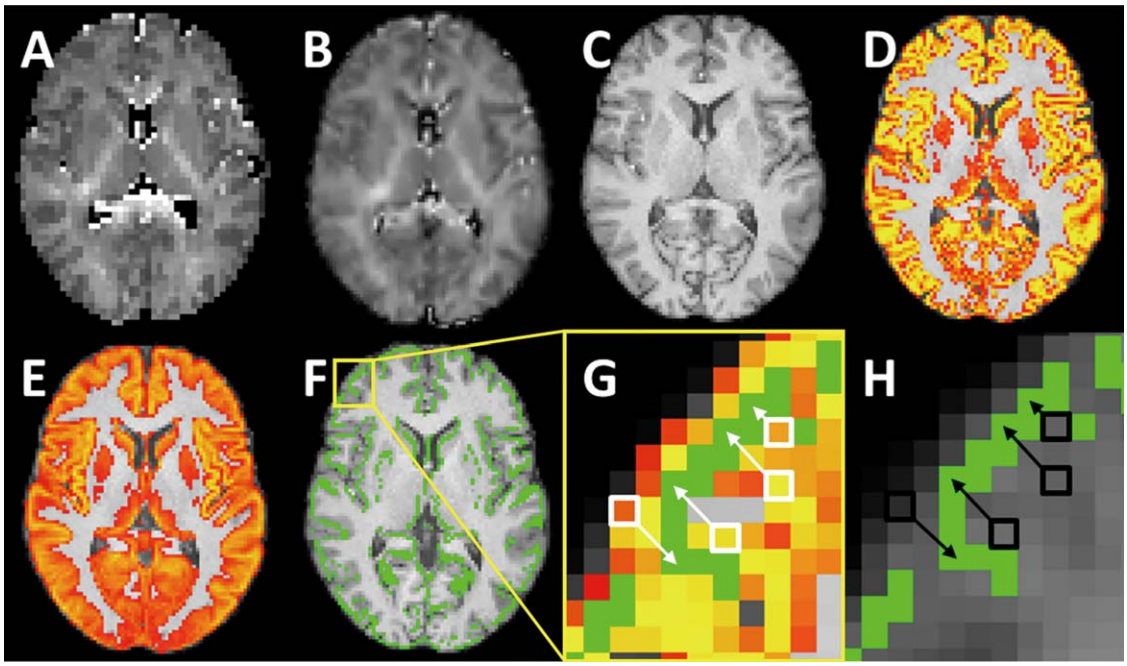

Figure 1.

Steps for processing gray matter based spatial statistics. (A) ICVF map. (B) Normalized ICVF map. (C) 3D T1-weighted image. (D) Cortical tissue probability map. (E) Population mean cortical tissue probability map. (F) Skeletonized cortical map overlaid on a template. (H) Illustration of the region contained in the yellow square in F. The cortical probability map from D is transformed into the template space. Once aligned, the cortical voxels near the skeleton (shown in green) are identified (white squares). Data from these voxels are then projected onto the group skeleton for comparison (white arrows). (H) After aligning the ICVF map in A to the template, ICVF data from the voxels identified in G are projected onto the skeleton. This process is repeated for the other diffusion parameter maps. [Color figure can be viewed at wileyonlinelibrary.com]

Image processing was performed using the FMRIB Software Library version 5.0.9 (FSL) [Jenkinson et al., 2012]. A schematic of the processing pipeline is shown in Figure 1. First, the skull was removed [Smith, 2002] from each subject's 3D-T1WI volume to exclude non-brain voxels from further consideration. Then, each skull-stripped 3D-T1WI was affine- and nonlinearly aligned to a common space (MNI152 brain at 1-mm resolution) using FLIRT [Jenkinson et al., 2002] and FNIRT [Jenkinson et al., 2012], respectively.

Next, FAST [Zhang et al., 2001], included in FSL, was used to bias correct and segment the 3D-T1WI of every subject into three tissue classes (GM, WM, and CSF). A mean GM map was created from the GM images, which was skeletonized to retain the core of highly probable cortical voxels at the center of the GM (mean GM skeleton). A mean GM skeleton mask was created from the mean GM skeleton at a threshold of 0.2. Subsequently, a GM skeleton distance map was produced from the mean GM image, and GM skeleton masks were delineated using the "distancemap" program implemented in FSL [Smith et al., 2006]. Each voxel in the GM skeleton distance map contains a value encoding the distance to the nearest skeleton point [Smith et al., 2006].

Finally, after the b0 maps from each of the subjects were affine-aligned to their 3D-T1WI (epi-reg), diffusion parameter maps for the subjects were affine- and nonlinearly aligned into a common space (MNI152 brain at 1-mm resolution) [Jenkinson et al., 2012]. The aligned diffusion parameter maps obtained from each subject were then projected onto the mean GM skeleton map. This was achieved by searching in a direction perpendicular to the cortical skeleton and identifying maximally probable cortical voxels in each of the spatially transformed cortical probability maps, such that only data from nearby voxels with maximal cortical probability were kept and projected onto the skeleton. The aim here was to account for residual misalignment between subjects after the initial nonlinear registration.

Diffusion Metric ROI Analysis

We measured the average diffusion metrics of the GM skeleton of each subject using the Harvard-Oxford cortical and subcortical structural atlas on MNI152 space. The Harvard–Oxford cortical structural atlas provides a regional parcellation comprising 96 regions (48 regions × 2, left

and right), and 17 regions in the subcortical structural atlas (8 from the cerebral cortex, thalamus, caudate, pallidum, hippocampus, amygdala, and accumbens × 2, left and right; and the brain stem). Each diffusion metric was averaged over all GM skeleton voxels comprising a given region delineated by this atlas. This was repeated independently for all regions to yield a regional representation for each diffusion metric.

GM Volume Analysis with Voxel-Based Morphometry (VBM)

GM volume was examined using voxel-based morphometry (VBM). This was conducted using the Statistical Parametric Mapping (SPM) 8 software for Windows (available at: http://www.fil.ion.ucl.ac.uk/spm/software/spm8/) running on a Matlab 2014a platform (The MathWorks, Natick, MA, https://www.mathworks.com/products/matlab.html). The 3D-T1 weighted images were segmented into GM, WM, and CSF (unified segmentation model; [Ashburner and Friston, 2005]). Although the tissue segmentation of T1WI was already been performed in the diffusion metric voxel-wise analysis (described in the previous section), tissue segmentation was performed again using the unified segmentation model, which is a method optimized for VBM-DARTEL. The GM maps were then spatially normalized with Diffeomorphic Anatomical Registration using the Exponentiated Lie algebra (DARTEL) [Ashburner, 2007]. Subsequently, images were resampled to MNI space in 1.5-mm cubic resolution. Resulting GM probability maps were smoothed using an 8-mm full width at half maximum (FWHM).

Surface-Based Cortical Thickness Analysis

Surface-based cortical thickness analyses were performed using the FreeSurfer software, version 5.0.0 (Massachusetts General Hospital, Harvard Medical School; available at: http://surfer.nmr.harvard.edu) the details of which have been described elsewhere [Fischl and Dale, 2000; Fischl et al., 1999].

The implemented processing pipeline included the following: motion correction, removal of non-brain tissue, transformation to the Talairach reference space, segmentation of the subcortical WM and deep GM volumetric structures, intensity normalization, tessellation of the GM-WM boundary, automated topology correction, and surface deformation following intensity gradients to optimally place the gray/white and gray/cerebrospinal fluid borders at the location where the greatest shift in intensity defines the transition to the other tissue class. Misclassification of tissue types was corrected with minimal manual adjustment by one of the authors (R.U.) who was blind to the patients' diagnoses and clinical information. Cortical thickness was calculated as the shortest distance between the GM/WM boundary and the corresponding pial surface at each vertex across the cortical mantle. The maps were smoothed using a surface-based Gaussian kernel of 15-mm FWHM and averaged across the subjects. In addition, estimated total intracranial volume (eTIV), total GM volume, and total WM volume were calculated from the Freesurfer processing stream. These volumes were extracted from the aseg.stats file, which is an output of the recon-all workflow in Freesurfer (see https://surfer.nmr.mgh.harvard.edu/fswiki/MorphometryStats).

Statistical Analysis

All statistical analyses were performed using the Statistical Package for the Social Sciences for Windows, Release 20.0 (SPSS, Chicago, IL). All demographic and clinical variables were normally distributed, as quantified using the Kolmogorov–Smirnov test. Demographic and clinical data were analyzed with Student's *t*-test for continuous variables and the Chi Square test for categorical variables. Statistical significance was set to $P < 0.05$.

ROI Analysis

To identify significant patient-control differences in ROI-averaged diffusion measures, an independent two-sample *t*-test was performed for each ROI. This resulted in 1,130 independent tests (113 ROIS × 10 diffusion metrics). The 10 diffusion metrics measured at each ROI were as follows: FA, MD, AD, RD, ICVF, OD, ISOVF, MK, AK, and RK. Bonferroni correction was used to correct for multiple comparisons across the 1,130 tests, thus mandating a corrected significance level of $P < 0.05/1{,}130 = 0.0000442$). Effect sizes were measured with Cohen's d [Cohen, 1992].

In addition, we performed Linear discriminant analysis (LDA) to test whether subject diagnosis (patient or control) could be predicted based on a linear combination of regional diffusion metrics. LDA procedures are described in detail in Supporting Information Methods.

Pearson's correlation coefficient was used to test for any linear associations between the diffusion metrics and clinical variables, including disease duration and disease severity, as measured by the motor scores of the UPDRS-III. The false discovery rate (FDR) correction was used to correct for multiple comparisons.

GBSS, VBM, Surface Based Cortical Thickness Analysis

For GBSS, the Randomize tool [Winkler et al., 2014] (FSL) was used to ascribe a family-wise error (FWE)–corrected *P*-value (pFWE) to each cluster of voxels comprising the GM skeleton. The TFCE option was used in Randomize to avoid selection of an arbitrary cluster-forming threshold, and 5,000 permutations were generated to provide an empirical null distribution of maximal cluster size [Smith and Nichols, 2009]. Voxel-wise statistics of the diffusion metrics for group differences [all PD (n = 30) vs. healthy controls, right-sided onset PD (n = 17) vs. left-sided onset PD (n =

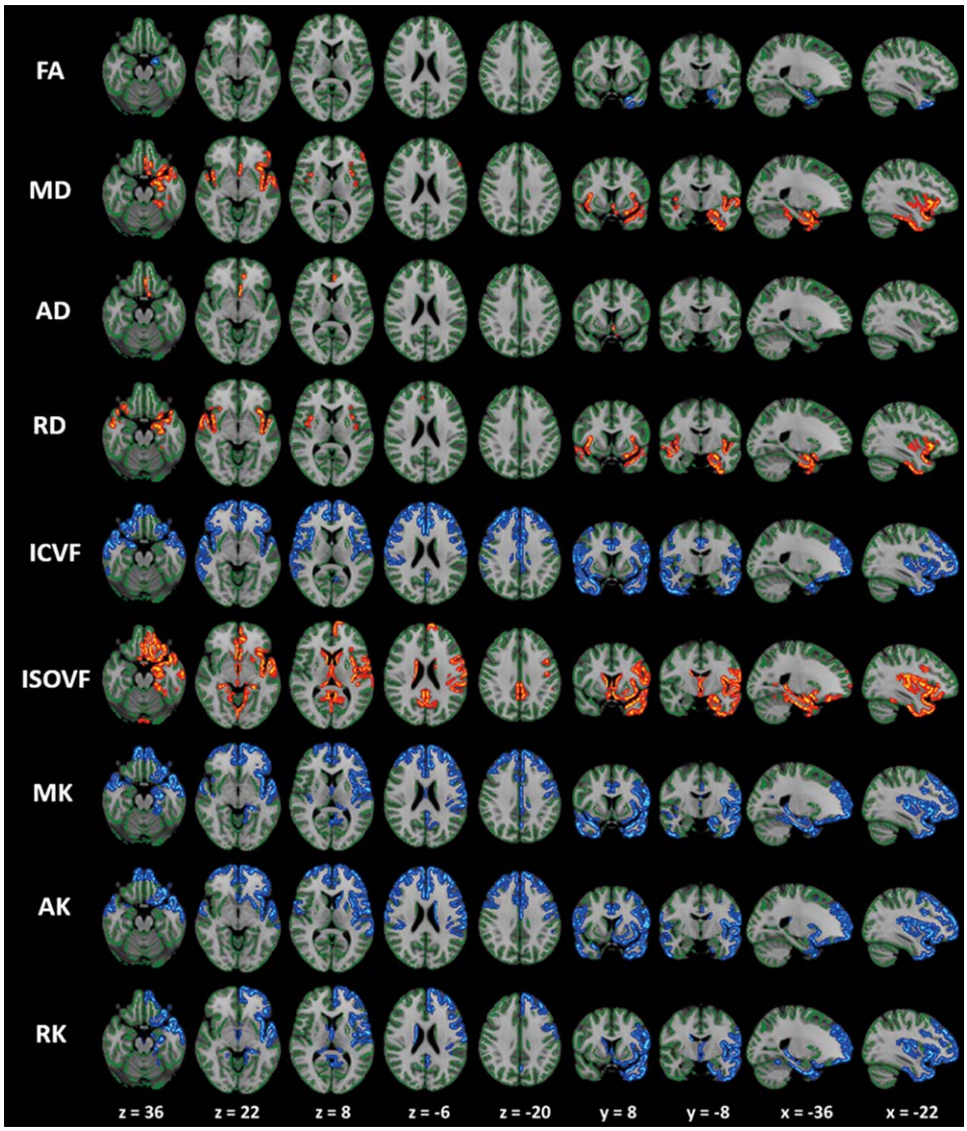

Figure 2.

Comparison of DTI, DKI and NODDI metrics between PD patients and controls. GBSS results showed reduced FA, ICVF, MK, AK, and RK (blue-light blue voxels), and increased MD, AD, RD, and ISOVF (red-yellow voxels) in PD patients when compared with age-matched healthy subjects. All images are displayed in Montreal Neurological Institute space using neurological convention. In patients with PD, cortical GM in the frontal, temporal, limbic, and paralimbic areas demonstrated significantly reduced MK, AK, RK, and ICVF when compared with the control group (GBSS analysis). Regions where significant changes in the conventional DTI parameters (FA, AD, and RD) occurred were noticeably smaller than those where significant changes in MK, AK, RK, and ICVF were observed. To aid visualization the results (corrected $P < 0.05$) are thickened using the fill script implemented in FSL. AD, axial diffusivity; AK, axial kurtosis; FA, fractional anisotropy; MD, mean diffusivity; MK, mean kurtosis; OD, orientation dispersion index; RD, radial diffusivity; RK, radial kurtosis; ICVF, intracellular volume fraction; ISOVF, isotropic volume fraction. [Color figure can be viewed at wileyonlinelibrary.com]

11), healthy controls (n = 28) vs. right-sided onset PD (n = 17), healthy controls (n = 28) vs. left-sided onset PD patients (n = 11)] were tested in the general linear model (GLM) framework with the unpaired t-test, using the Randomize tool with nonparametric permutation testing. A pFWE of <0.05 was considered significant for GBSS. The Randomize tool was also used to examine the relationship between diffusion metrics and disease duration, and the motor score of the UPDRS-III using multiple linear regression analysis (pFWE <0.05, corrected for gender and age).

In the VBM analysis, GM volume was compared between PD patients and healthy controls using GLM Analysis of Co-variance (ANCOVA), which included age, sex, and total intracranial volume as covariates. GM volume comparisons were corrected for multiple comparisons using the family wise error (FWE) rate set at $P < 0.05$. Correlations were used to assess relationships between regional GM volume and disease duration, and the motor score of the UPDRS-III by multiple regression analysis, which corrected for multiple comparisons using a FWE correction set at $P < 0.05$.

Cortical thickness was assessed for between-group differences at each vertex of the surface using a GLM controlling for age, gender, and eTIV. Correlations between cortical thickness and disease duration, as well as the motor score of the UPDRS-III were also modeled while controlling for age, gender and eTIV. In all vertex-wise analyses, the level of statistical significance was evaluated using a cluster-wise P (CWP) value correction procedure for multiple comparisons with cluster-based Monte–Carlo simulation using 10,000 permutations. Clusters with CWP value <0.05 were considered statistically significant.

RESULTS

Participants

No significant differences were observed in age and sex between all PD patients and healthy controls or right-sided PD patients and left-sided PD patients or healthy controls and right-sided PD patients or healthy controls and left-sided PD patients. The initial symptoms of PD had emerged on the left side of the body in 11 patients, the right side in 17 patients, and on both sides in two patients. Table I summarizes the demographic and clinical data of the PD patients and healthy controls included in this study.

GM Microstructure Abnormalities in PD (NODDI, DKI, DTI)

NODDI

GBSS analysis. In the GBSS analysis, cortical GM in the frontal, temporal, limbic, and paralimbic areas displayed significantly reduced ICVF and increased ISOVF in PD patients when compared with healthy controls (Fig. 2; Supporting Information Tables I and II). Significant decreases in ICVF in parts of the parietal lobe, and increases in ISOVF in the left and right caudate nuclei and the left putamen were also observed. Increased ISOVF area was broader in the left hemisphere than the right hemisphere. No significant differences in OD were observed between the PD patients and healthy subjects. There were no significant differences in NODDI parameters between right-sided onset PD patients and left-sided onset PD patients or healthy subjects and right-sided onset PD patients or healthy subjects and left-sided onset PD patients.

ICVF and OD measured in the frontal, temporal, limbic, basal ganglia, and paralimbic areas was negatively correlated with UPDRS-III scores in the PD patients, whereas ISOVF of the basal ganglia was positively correlated with UPDRS-III scores (Fig. 3; Supporting Information Tables III and IV).

ROI analysis. In the ROI analysis, significantly decreased ICVF was found in the bilateral paracingulate and cingulate gyri (Fig. 4; Table III).

In the ROI-based correlation analysis, significant negative correlations with UPDRS-III scores were observed for ICVF and OD of the left inferior frontal gyrus (IFG) pars triangularis (Tr), as well as the OD of the left central opecular cortex (COC). In addition, ISOVF of the right hippocampus (HCP) was positively correlated with the UPDRS-III scores. No significant correlations were detected between disease duration and the NODDI parameters.

DKI

GBSS analysis. In the GBSS analysis, cortical GM in the frontal, temporal, limbic, and paralimbic areas displayed significantly reduced MK, AK, and RK in PD patients when compared with the healthy control group (Fig. 2; Supporting Information Tables I and II). Other findings included decreased MK, AK, and RK in parts of the parietal lobe; decreased AK in the left caudate nucleus and the left putamen; and reduced RK in the right putamen. Decreased MK and RK area were broader in the left hemisphere than in the right hemisphere. There were no significant differences in DKI parameters between right-sided onset PD patients and left-sided onset PD patients or healthy subjects and right-sided onset PD patients or healthy subjects and left-sided onset PD patients.

In the GBSS analysis, the MK, AK, and RK of the frontal, temporal, basal ganglia, limbic, and paralimbic areas showed negative correlations with UPDRS-III scores in patients with PD (Fig. 3; Supporting Information Tables III and IV).

ROI analysis. In the ROI analysis, the following significant decreases were detected: MK and AK in the anterior division of the left superior temporal gyrus (STG); MK, AK, and RK of the left frontal operculum cortex (FOC); and RK of the left planum polare (Fig. 4; Table III).

In the ROI-based correlation analysis, the following significant negative correlations were found with UPDRS-III scores: MK and AK of the left IFGTr; MK and RK of the right IFGTr; RK of the right FOC; RK of the posterior division of the right middle temporal gyrus (MTG); and RK of the left caudate. No significant correlations were detected between disease duration and the DKI parameters.

DTI

GBSS analysis. In the GBSS analysis, the area where there were significant differences in conventional DTI

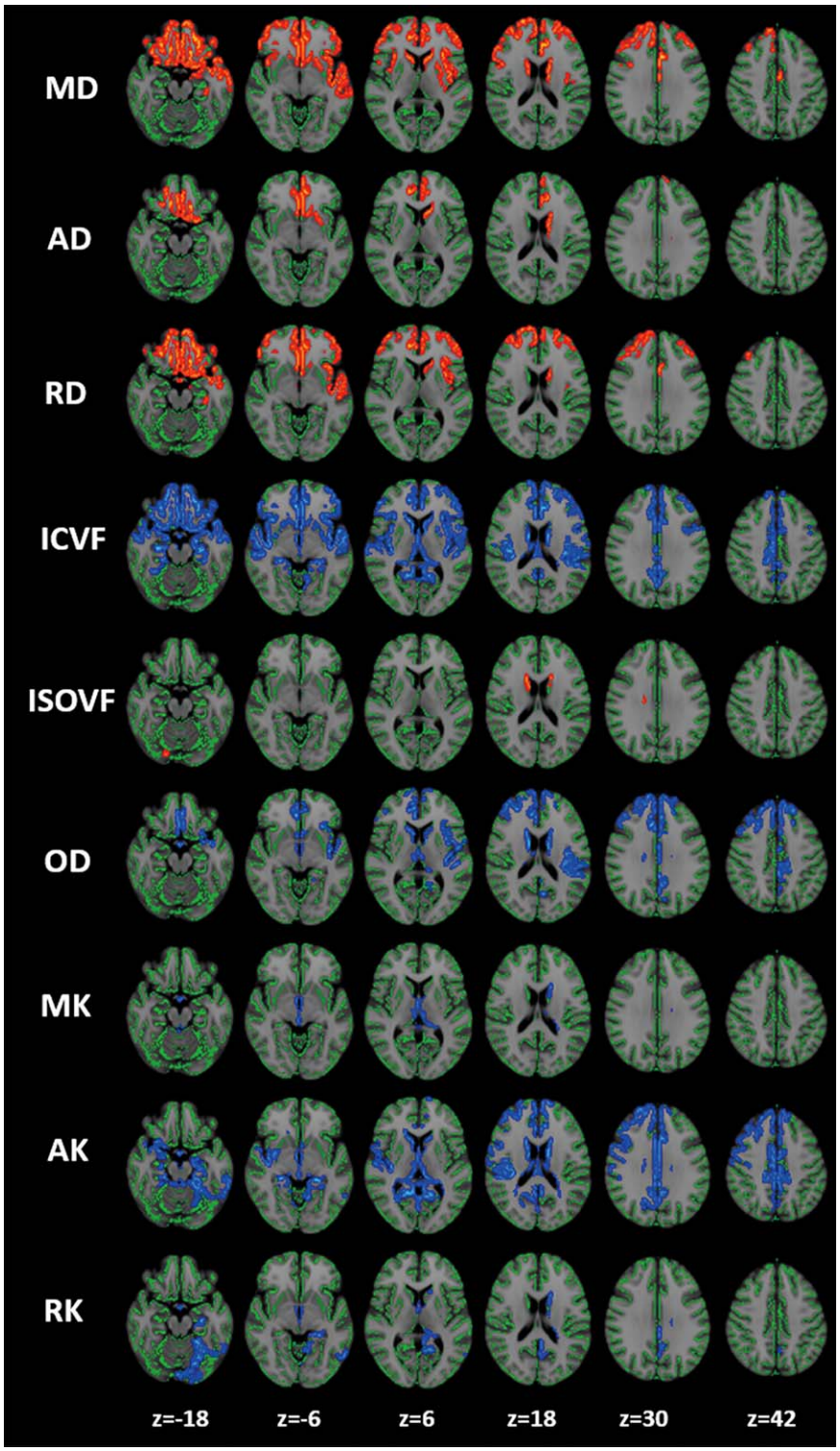

Figure 3.

Relationship between diffusion MRI parameters and disease severity according to Unified Parkinson's Disease Rating Scale (UPDRS)-III–motor subscale score. GBSS analysis identified a significant correlation between UPDRS-III–motor score and the diffusion MRI parameters of the cortical GM in the frontal, temporal, limbic, and paralimbic areas, as well as in the basal ganglia ($P < 0.05$, corrected for multiple comparisons, gender and age at the time of MRI). Red–yellow voxels demonstrate a significant positive correlation between the UPDRS-III–motor score and diffusion MRI parameters. Blue–light blue voxels demonstrate a significant negative correlation between the UPDRS-III–motor score and diffusion MRI parameters. To aid visualization the results (corrected $P < 0.05$) are thickened using the fill script implemented in FSL. AD, axial diffusivity; AK, axial kurtosis; FA, fractional anisotropy; MD, mean diffusivity; MK, mean kurtosis; OD, orientation dispersion index; RD, radial diffusivity; RK, radial kurtosis; ICVF, intracellular volume fraction; ISOVF, isotropic volume fraction. [Color figure can be viewed at wileyonlinelibrary.com]

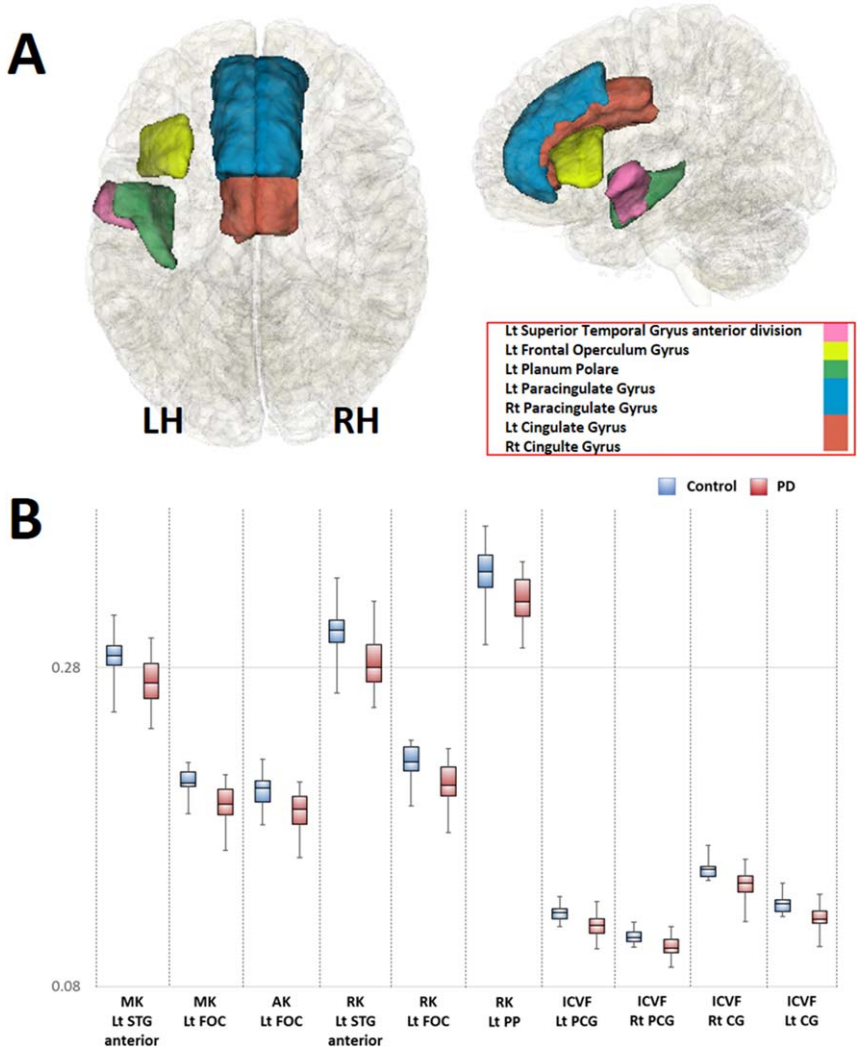

Figure 4.

Regions where the values of dMRI parameters in the PD group were significantly different from their respective values in the healthy group (A), and box plots of diffusion MRI parameters in these regions (B). (A) Regions where dMRI parameters were significantly reduced are shown. The bilateral cingulate gyrus, bilateral paracingulate gyrus, left superior temporal gyrus anterior part, the left frontal opeculum cortex, and left planum polare are represented in light blue, red, pink, yellow, and green, respectively. LH, left hemisphere; RH, right hemisphere. B) When compared with the healthy group (light blue), MK and AK of the left superior temporal gyrus (STG) anterior division; MK, AK, and RK of the left frontal operculum cortex (FOC); RK of the left planum polare (PP); and ICVF of the bilateral paracingulate gyrus (PCG) and cingulate gyrus (CG) were significantly reduced in the PD group (light red). Plots indicate median values, and boxes include the upper and lower quartiles. Whiskers represent the lowest (highest) values within the 1.5 interquartile range in the box. AD, axial diffusivity; AK, axial kurtosis; FA, fractional anisotropy; MD, mean diffusivity; MK, mean kurtosis; OD, orientation dispersion index; RD, radial diffusivity; RK, radial kurtosis; ICVF, intracellular volume fraction; ISOVF, isotropic volume fraction; CG, Cingulate Gyrus; FOC, Frontal Operculum Cortex; PCG, Paracingulate Gyrus; STG, Superior Temporal Gyrus. [Color figure can be viewed at wileyonlinelibrary.com]

parameters, including FA, AD, and RD, were noticeably smaller than, and mostly circumscribed to, areas with significantly lower MK, AK, RK, and ICVF. Specifically, when compared with the control group, PD patients displayed significantly reduced FA in the left temporal, left limbic, and paralimbic areas; significantly increased MD in left frontal, left temporal, left limbic, and paralimbic areas; significantly increased AD in left frontal, left limbic, and paralimbic areas; and significantly increased RD in the bilateral frontal, limbic, and paralimbic areas (Supporting

TABLE III. Comparison of diffusion MRI parameters in the anatomic regions where significant differences were observed between PD patients and healthy subjects

Diffusion parameters	Regions	CC	PD	*P* value	*t* value	Cohen's *d*
MK	Lt STG anterior	0.29 (0.012)	0.27 (0.014)	1.4×10^{-5}	4.76	1.28
	Lt FOC	0.21 (0.075)	0.19 (0.011)	9×10^{-7}	5.53	1.49
AK	Lt FOC	0.25 (0.0080)	0.24 (0.012)	6.2×10^{-5}	4.33	1.16
RK	Lt STG anterior	0.30 (0.014)	0.28 (0.017)	9.3×10^{-6}	4.88	1.31
	Lt FOC	0.22 (0.0093)	0.21 (0.013)	1.1×10^{-5}	4.83	1.30
	Lt PlanumPolare	0.34 (0.015)	0.32 (0.014)	3.2×10^{-5}	4.52	1.21
ICVF	Lt PCG	0.13 (0.0049)	0.12 (0.0068)	6.7×10^{-6}	4.97	1.34
	Rt PCG	0.11 (0.0041)	0.10 (0.0061)	1.7×10^{-5}	4.71	1.27
	Lt CG	0.15 (0.0049)	0.14 (0.0082)	8.9×10^{-6}	4.89	1.32
	Rt CG	0.13 (0.0051)	0.12 (0.0064)	3.1×10^{-6}	5.18	1.39

Abbreviation; (Parameters) AD, axial diffusivity; AK, axial kurtosis; FA, fractional anisotropy; MD, mean diffusivity; MK, mean kurtosis; OD, orientation dispersion index; RD, radial diffusivity; RK, radial kurtosis; ICVF, intracellular volume fraction; ISOVF, isotropic volume fraction; (Anatomical part) Lt, left; Rt, right; CG, Cingulate Gyrus; FOC, Frontal Operculum Cortex; PCG, Paracingulate Gyrus; STG, Superior Temporal Gyrus.

Information Tables I and II). There were no significant differences in DTI parameters between right-sided onset PD patients and left-sided onset PD patients or healthy subjects and right-sided onset PD patients or healthy subjects and left-sided onset PD patients.

In the GBSS analysis, MD, AD, and RD of the frontal, temporal, limbic, and paralimbic areas and the basal ganglia showed a positive correlation with UPDRS-III scores in patients with PD (Fig. 3; Supporting Information Tables III and IV).

ROI analysis. The ROI analysis revealed no significant differences in conventional DTI parameters. In the ROI-based correlation analysis, only the AD of the right hippocampus (HCP) and the left amygdala (AMY) were positively correlated with the UPDRS-III scores. No significant correlations were detected between disease duration and the DTI parameters (Fig. 5).

VBM and Surface-Based Cortical Thickness

There were no significant differences in total brain, GM, and WM volumes. No statistically significant differences were found between PD patients and controls in GM volumes and cortical thickness. No significant correlations were found between disease duration, (UPDRS)-III score, and GM volume and thickness in PD patients

Prediction of Diagnosis

LDA predicted diagnosis with the greatest accuracy, with a classification accuracy of 76.7% (sensitivity, 71.0%; specificity, 82.4%) when trained based on MK measurements from only three regions (left frontal operculum, left superior temporal gyrus, and left planum polare). LDA classification accuracies for the other diffusion metrics are shown in Table IV in the case of a three-feature classifier; as seen in the table, ICVF, AK, and RK were able to predict diagnosis with an accuracy exceeding 70%, whereas the tensor-derived diffusion measures yielded accuracies of 60%–70%. Table IV also lists the specific regions that provided the greatest discriminatory power between the patients and controls. Measurements in the frontal, temporal, and limbic regions provided the greatest power to predict diagnosis. LDA classification accuracy was typically greatest when using three regions (Supporting Information Fig. 1).

DISCUSSION

We used dMRI, VBM, and surface-based cortical thickness analyses to examine the microstructure of the cortical and subcortical structures in a group of idiopathic PD patients and healthy controls. Abnormalities in dMRI parameters were detected within the frontal, temporal, limbic, and paralimbic areas, and the striatum of the idiopathic PD patients. The voxel-wise GBSS results identified widespread reductions in DKI parameters (MK, AK, and RK) and a NODDI parameter (ICVF). In addition, the LDA results indicated that MK and ICVF maximized the prediction accuracy of diagnostic status. In contrast, no gray matter differences were detected with the traditional VBM or surface-based cortical thickness analyses suggesting that, as expected, DKI and NODDI modalities offer greater sensitivity in the detection of cortical abnormalities in idiopathic PD when compared with traditional MR modalities. This was further reinforced by the correlation analyses, which revealed strong relationships between DKI and NODDI metrics in significant clusters and UPDRS-III scores, reflecting the severity of motor impairments. Therefore, abnormalities in dMRI parameters were clinically meaningful and reflected the markers of motor symptom severity in PD.

Our VBM and cortical thickness results are in agreement with previous studies reporting no between-group

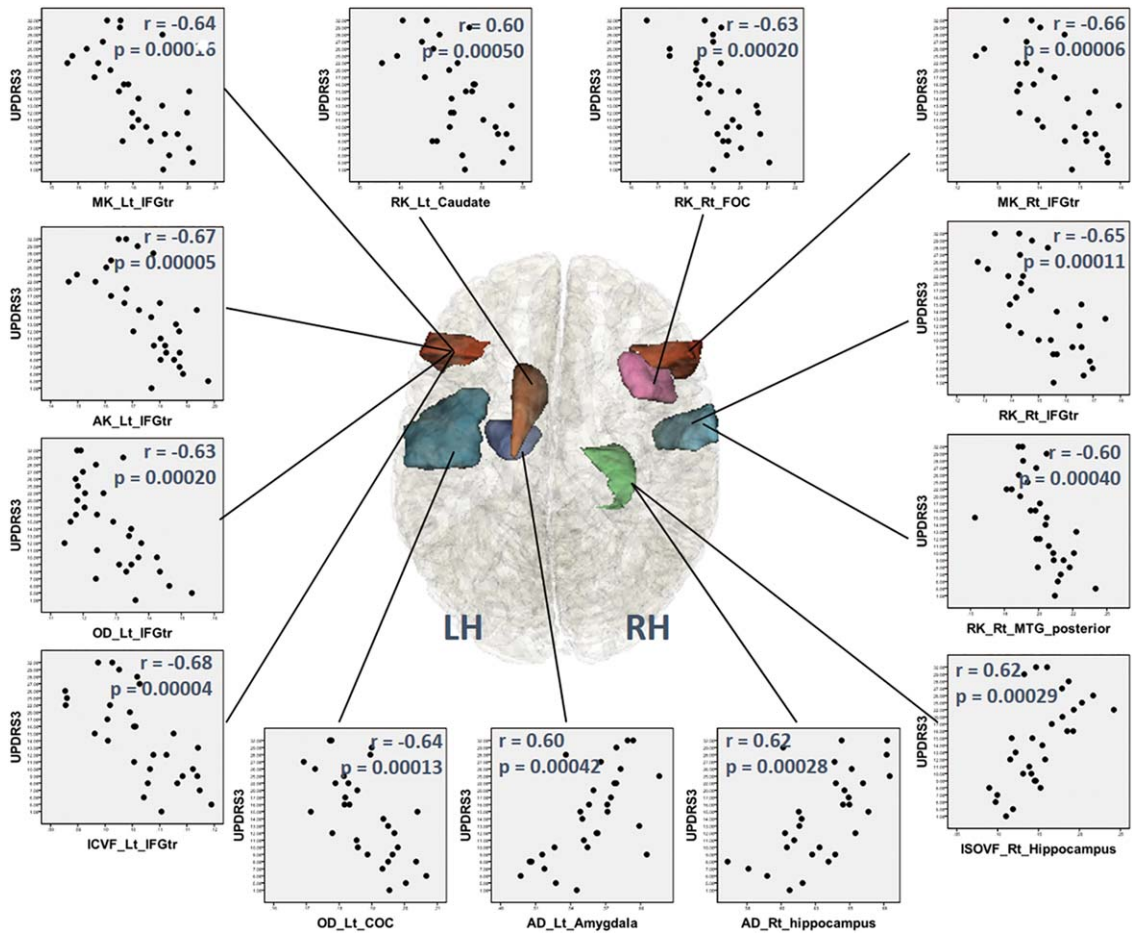

Figure 5.

Regions where dMRI parameters were significantly correlated with the Unified Parkinson's Disease Rating Scale (UPDRS)-III-motor subscale scores in the PD group using ROI analysis; scatter diagrams of these regions. MK, AK, ICVF, and OD of the left inferior frontal gyrus (IFG) pars triangularis (Tr); MK and RK of the right IFGTr, OD of the Lt central opercular cortex (COC); RK of the right frontal opercular cortex (FOC); RK of the right middle temporal gyrus (MTG) posterior division; and RK of the left caudate showed significant negative correlations with UPDRS-III scores. ISOVF and AD of the right hippocampus and AD of the left amygdala (AMY) showed positive correlations with UPDRS-III scores. AD, axial diffusivity; AK, axial kurtosis; FA, fractional anisotropy; MD, mean diffusivity; MK, mean kurtosis; OD, orientation dispersion index; RD, radial diffusivity; RK, radial kurtosis; ICVF, intracellular volume fraction; ISOVF, isotropic volume fraction; COC, central opecular cortex; FOC, Frontal Operculum Cortex; IFGTr, inferior frontal gyrus pars triangularis; MTG, middle temporal gyrus; STG, Superior Temporal Gyrus. [Color figure can be viewed at wileyonlinelibrary.com]

differences in brain atrophy or cortical thinning [Cerasa et al. 2011; Feldmann et al. 2008; Messina et al. 2011; Paviour et al. 2006; Rizzo et al. 2008; Seppi and Poewe, 2010]. VBM and surface-based cortical thickness measures are considered as indirect indications of neuronal loss. In addition, although PD patients displayed abnormalities in DTI parameters (FA, MD, AD, and RD), the deficits were more circumscribed when compared with the more widespread abnormalities identified with the DKI and NODDI parameters. Thus, DTI appears to provide less sensitivity compared with the higher-order DKI and NODDI parameters. DKI extends conventional DTI measures by detecting microstructural changes in both anisotropic (WM) and isotropic tissues (GM) [Jensen et al., 2005; Lu et al., 2006]. In addition, NODDI can characterize the microstructure of dendrites and axons in GM and WM and thus, provides information on pathological changes that are more specific than those provided by conventional GM measures [Zhang et al., 2012]. Accurate tissue estimation with these high-order diffusion models may thus allow the detection of changes in neurite structure preceding neuronal loss in GM.

TABLE IV. Performance of the linear discriminant models for prediction of PD diagnosis

		Accuracy (%)/SE (%)	Sensitivity (%)/SE (%)	Specificity (%)/SE (%)	First region (*P* value)	Second region (*P* value)	Third region (*P* value)
DTI	FA	61.9/1.6	64.4/2.5	59.4/2.3	Lt Temporal Pole (8×10^{-4})	Rt Superior Temporal Gyrus (9.1×10^{-4})	Rt Central Opecular Cortex (1.4×10^{-3} 0.0014)
	MD	69.0/1.5	70.6/2.2	67.4/2.2	Rt Middle Temporal Gyrus (9.3×10^{-5})	Lt Temporal Fusiform Cortex (1.1×10^{-4})	Lt Supracalcarine Cortex (5.5×10^{-4})
	AD	65.8/1.4	67.7/2.2	63.9/2.1	Rt Middle Temporal Gyrus (1.3×10^{-4})	Lt Temporal Fusiform Cortex (1.5×10^{-4})	RtSubcallsal Cortex (2.2×10^{-4})
	RD	63.6/1.5	69.0/2.4	58.2/2.1	Rt Middle Temporal Gyrus (1.2×10^{-4})	Rt Superior Temporal Gyrus (4.4×10^{-4})	Rt Central Opecular Cortex (5.3×10^{-4})
NODDI	ICVF	74.3/1.3	74.0/2.0	74.6/1.9	Rt Cingulate Gyrus (3.1×10^{-6})	Lt Paracingulate Gyrus (6.7×10^{-6})	Lt Cingulate Gyrus (8.9×10^{-6})
	OD	61.3/1.3	59.8/2.3	62.8/2.1	Lt Parietal Operculum Cortex (2.8×10^{-3})	Rt Caudate (4.7×10^{-3})	Lt Postcentral Gyrus (6.8×10^{-3})
	ISOVF	63.6/1.4	61.0/2.0	66.2/2.1	Lt Middle Temporal Gyrus (2.3×10^{-4})	Left Amygdala (3.3×10^{-4})	Lt parahippocampal Gyrus (3.3×10^{-4})
DKI	MK	76.7/1.2	71.0/1.9	82.4/1.5	Lt Frontal Operculum Cortex (8.8×10^{-7})	Lt Superior Temporal Gyrus (1.4×10^{-5})	Lt Planum Polare (5.9×10^{-5})
	AK	70.1/1.5	65.7/2.1	74.5/2.1	Lt Frontal Operculum Cortex (2.4×10^{-5})	Rt Superior Temporal Gyrus (6.2×10^{-5})	Lt Inferior Frontal gyrus (9.5×10^{-5})
	RK	73.9/1.5	66.2/2.1	81.6/2.0	Lt Superior Temporal Gyrus (9.3×10^{-6})	Lt Frontal Operculum Cortex (1.1×10^{-5})	Lt Planum Polare (3.2×10^{-5})

abbreviations: AD, axial diffusivity; AK, axial kurtosis; FA, fractional anisotropy; MD, mean diffusivity; MK, mean kurtosis; OD, orientation dispersion index; RD, radial diffusivity; RK, radial kurtosis; ICVF, intracellular volume fraction;, ISOVF, isotropic volume fraction; Rt, right; Lt, left; SE, standard error.

The distribution of abnormalities in dMRI parameters overlaps with areas of cortical LBs and LNs previously found in patients with symptomatic PD, corresponding to Braak's stages IV (thalamus and anteromedial temporal, and paralimbic cortices) and V (striatum, prefrontal cortex, temporal cortex, insular, and parietal cortex). LNs and LBs are deposited in the neurons, axons, and dendrites and are closely related to neuronal loss and changes in the neurite structure [Jellinger, 2012]. Axonal accumulation of LNs, accompanied by changes in the axon structure (for instance, dystrophic neurites) are thought to endanger the functional integrity and survival of neurocytes by inhibiting axonal transport, which eventually leads to neurodegeneration [Morfini et al., 2009; Perlson et al., 2010]. In other words, structural neurite changes associated with LN deposition precede neuronal loss. Moreover, alpha-synuclein—a main component of LNs—has been reported to inhibit neurite outgrowth and branching [Koch et al., 2015]. Thus, our findings of reduced ICVF (neurite density), reduced MK, AK, and RK (tissue heterogeneity and complexity), and increased ISOVF (free water compartment), may reflect the sparse neurite structure and neuronal loss caused by inhibition of neurite outgrowth and branching inhibition in the gray matter. On the other hand, studies using DKI in PD mouse models (α-synuclein-overexpressing transgenic mice) have shown that the kurtosis parameters are increased in the SN, striatum, thalamus, hippocampus, and cingulate gyrus of PD model mice, and that levels of α-synuclein accumulation in these regions positively correlate with kurtosis parameters [Khairnar et al., 2015a,b]. However, in contrast to results from previous PD mouse model studies, human PD studies, including this study and others [Surova et al., 2016], have shown significantly reduced kurtosis parameters in the basal ganglia, thalamus and cortical GM. This discrepancy may be due to differences in pathological changes between human PD and α-synuclein-overexpressing transgenic mice. In human PD, neuronal loss and structural neurite alterations occur as α-synuclein deposits [Jellinger, 2012]. In contrast, α-synuclein is overexpressed throughout the brain, but no appreciable loss of neurons occurs in α-synuclein-overexpressing transgenic mice [Chesselet et al., 2012; Delenclos et al., 2014].

By training a simple linear classifier, we were able to predict an individual's diagnostic status with modest accuracy (~76%) based on regional variation in patterns of GM loss inferred from DTI, NODDI, and DKI parameters. In particular, a linear discriminant function was trained independently for each parameter using cross-validation involving 10 held-out individuals per fold. A linear classifier was chosen because of the modest size of our sample. The cross-validation procedure used to evaluate classification accuracy involved holding out multiple individuals (5 patients and 5 controls). This has been shown to provide less biased and more stable classification accuracy estimates than leave-one-out methods [Varoquaux et al., 2017]. The most accurate prediction of diagnostic status was achieved with the MK parameter of DKI (76.70%) and

the ICVF parameter of NODDI (74.30%). DTI performed substantially poorer, with no DTI parameter yielding an accuracy exceeding 70%. This provides further evidence of the increased sensitivity of NODDI to Lewy-body pathology, relative to classic parameters derived from DTI. Variation in GM loss in the cingulate and paracingulate gyri was most informative for the prediction of diagnostic status when prediction was based on ICVF, whereas GM loss in the frontal operculum and temporal gyrus was most informative with respect to DKI. Future studies might consider a multivariate classifier in which NODDI and DKI parameters are combined to inform prediction, and prediction of patient outcome, which provides high clinical utility.

We identified significant correlations between motor deficits and dMRI parameters in the frontal, temporal, limbic and paralimbic areas, striatum, and thalamus, which is consistent with a previous pathological study showing a correlation between Braak's stage of Lewy-related pathology and PD severity [Braak et al. 2005]. Furthermore, it is thought that the basis of the pathophysiology of PD is primarily related to disruption of the cortico-striatal and limbic loop [Braak et al., 2004]. In the present study, motor symptom severity was correlated to dMRI parameters in the cortical and limbic loops and may thus reflect abnormalities in hubs within these loops.

Some left hemispheric dominant asymmetry was evident in the spatial distribution of GM pathology in our sample; correlation analyses showed a tendency toward greater changes in the left cerebral hemisphere. In most PD patients, asymmetry in clinical symptoms from disease onset is remarkably evident and a unilateral predominance can persist over the course of illness [Djaldetti et al., 2006]. This clinical asymmetry has been associated with more severe contralateral nigrostriatal degeneration [Kempster et al., 1989]. In contrast, we found no significant differences in diffusion parameters between right- and left-sided onset PD patients or between healthy controls and right- or left-sided onset PD patients. Contralateral to the side of symptom onset, our asymmetrical result may relate to vulnerability in the left hemisphere of PD patients. In particular, several PD studies have suggested that the left nigrostriatal pathway is more affected than the right [Prakash et al., 2012; Scherfler et al., 2012]. Given this vulnerability of the left nigrostriatal pathway to neurodegeneration, it is possible that cortical degeneration in PD may also lateralize to the left side. Accordingly, PD-related cortical atrophy in the left hemisphere was reported in several studies [Bruck et al., 2004; Claassen et al., 2016; Jubault et al., 2011; Mak et al., 2015]. Although we did not detect significant cortical atrophy in PD, we found cortical changes predominantly in the left hemisphere, in agreement with prior studies.

Our finding of differences in AK, RK, and ISOVF in the striatum and thalamus between PD patients and healthy controls may relate to the progressive degeneration of nigrostriatal dopaminergic neurons. In particular, the thalamus and striatum are areas intimately linked to the degeneration of nigrostriatal dopamine nerves, which represent the center of the motor symptoms in PD, and correspond to Braak's stages IV and V, respectively [Braak and Del Tredici, 2008; Jellinger, 2012]. While previous studies have documented reduced ICVF and OD of the putamen [Kamagata et al. 2015], increased MK of the putamen and caudate nuclei [Wang et al. 2011], and reduced MK of the putamen [Surova et al. 2016] in patients with PD, no significant differences in ICVF nor OD of the putamen and caudate nuclei were observed in the present study. Conflicting findings between our study and previous work may relate to discrepancies in symptom severity or analyses applied across the studies. For example, the PD patient group in an earlier study [Wang et al., 2011], displayed higher motor symptom severity (UPDRS-III motor scores), than those in our study (Wang et al, mean = 33.6; this study, mean = 16.1). It is therefore possible that greater motor symptom severity underlies degeneration in the striatum. On the other hand, motor severity in the PD groups of the two aforementioned studies (Kamagata et al., mean- = 18.0; Surova et al., mean = 13.0; this study, mean = 16.1) [Kamagata et al., 2015; Surova et al., 2016], was similar to that in the present study. However, the striatum ROI was manually determined in all the previous studies [Kamagata et al., 2015; Surova et al., 2016; Wang et al., 2011], whereas automated voxel-wise measurements (GBSS) and an automated atlas-defined ROI were employed in the current study. In general, voxel-wise measurements and automated ROI methods, as applied in our study, are considered advantageous over manual ROI methods, because the analysis can be performed across the whole brain with minimal user bias [Johansen-Berg and Behrens, 2014].

We have demonstrated that voxel-wise gray matter analysis with GBSS enables the regional mapping and characterization of gray matter pathology in PD patients. A major problem in cortical GM measurement with diffusion MRI is PVE of the WM and CSF adjacent to the cortical GM [Lee et al., 2009]. It is difficult to obtain accurate measurements of the cortical GM, which is a very thin structure (a few mm) and has a complicated convolutional pattern, while avoiding PVE contamination with WM and CSF. Moreover, in the Voxel-based analysis (VBA), a common method of automated exploratory analysis, smoothing is generally performed to reduce individual differences [Lee et al., 2009], and this procedure further increases PVE of the WM and CSF [Lee et al., 2009]. As dMRI parameters of WM and CSF are very different from those of GM, the PVE of both WM and CSF greatly affect dMRI parameter measurements of the gray matter [Alexander et al., 2001]. When measurements are performed on patients with diseases associated with prominent brain atrophy, such as Alzheimer's disease, the CSF contamination increases due to increase in CSF regions in the cerebral sulci and ventricles owing to brain atrophy [Rose et al., 2008]. The GBSS method used in this study was developed by modifying

VBA for cortical analyses, and involves the aggregation of the dMRI parameters of regions surrounding a skeleton created at the center of the cortical GM, thereby minimizing PVE of the WM and CSF [Ball et al., 2013]. In addition, we excluded high-ISOVF regions (>90%) using ISOVF maps representing CSF compartments calculated by NODDI. Moreover, previous studies have proved that DKI is a more robust measurement when compared with conventional DTI with regards to the PVE of CSF [Falangola et al., 2008; Yang et al., 2013]. In the current study, the PVE of WM and CSF may not have been completely eliminated due to limited resolution (2-mm voxels were used). However, brain atrophy is generally mild in patients with Parkinson's disease, and no significant brain atrophy or cortical thinning was observed in the PD patients in this study. Therefore, it is unlikely that the effects of CSF contamination due to brain atrophy were particularly strong in the PD group.

There are some limitations to this study. First, the sample size was small. Large-scale, multicenter studies are needed to establish evidence for GM degeneration using DKI and NODDI. In addition, because this study was targeted at PD patients with relatively long disease duration, a longitudinal study of prodromal or early PD is required in order to confirm whether DKI and NODDI are effective as markers of disease progression. Second, this study did not evaluate clinical subtypes and non-motor symptoms of PD. PD is a complex neurodegenerative disease with broad-spectrum motor and non-motor symptoms. In addition, another neurodegenerative pathology, such as Alzheimer's disease, may exist simultaneously in PD patients. These findings may cause clinical heterogeneity of PD. PD clinically includes various motor symptom subtypes, such as tremor-dominant or akinetic-rigid dominant, and is often associated with non-motor symptoms, such as olfactory dysfunction or cognitive deficit. For evaluation of clinical subtypes and overlap with other neurodegenerative pathologies, the utility of functional imaging, such as dopamine transporter single-photon emission computed tomography or amyloid positron emission tomography, wearable biosensors, and serum, and CSF biomarkers has been reported in recent studies [Herman et al., 2014; Von Coelln and Shulman, 2016]. Therefore, future MRI studies should evaluate clinical subtypes and non-motor symptoms of PD and combine the results with those of other biomarkers. Third, it is currently not fully understood as to how changes in DKI and NODDI parameters relate to pathological changes in PD patients. DKI/NODDI remain as models for estimating the microstructure of brain tissue. Postmortem studies of human PD patients are necessary to address the relationship between DKI/NODDI parameters and pathological data. Finally, because the PD diagnoses were not histopathologically confirmed, the possibility of misdiagnosis remains. However, the validity of the diagnoses is supported by the observation that, 18 months or more after being scanned, all patients continued to respond satisfactorily to antiparkinsonian therapy and remained free of Atypical Parkinsonism. Finally, it is important to recognize that as with TBSS, GBSS does not provide sensitivity to detect peripheral effects that reside outside the skeleton, and the skeleton projection step can introduce bias to the projected parameters (Bach et al, 2014; Schwarz et al 2014; Zalesky, 2010).

In summary, we found that DKI and NODDI could detect cerebral GM abnormalities in PD patients more sensitively than conventional DTI, VBM, and surface-based cortical thickness analyses. Abnormalities were likely to reflect Lewy-related pathology, which is a hallmark of PD and may serve as a biomarker for early diagnosis and objective evaluation of its subsequent progression, given that a sensitive detection method is available. By providing a more sensitive index of brain pathology in PD, DKI, and NODDI might be useful for the early diagnosis of PD as well as the assessment of its motor deficits.

ACKNOWLEDGMENTS

We thank Nozomi Hamasaki and Syuji Sato, MR imaging technologists, for their skilful acquisition of data; Misaki Nakazawa, Syo Murata, and Kohei Tsuruta for their research assistance. This work was supported by the program for Brain Mapping by Integrated Neurotechnologies for Disease Studies (Brain/ MINDS) from Japan Agency for Medical Research and development (AMED); JSPS KAKENHI (JP16K19854); a research grant from Hitachi, Ltd. Christos Pantelis was supported by a National Health and Medical Research Council of Australia (NHMRC) Senior Principal Research Fellowship (ID: 1105825). Andrew Zalesky was supported by NHMRC Career Development Fellowship (GNT1047648). Maria Di Biase was supported by the Rotary Health Ian Scott PhD Scholarship in Mental Health.

REFERENCES

Alexander AL, Hasan KM, Lazar M, Tsuruda JS, Parker DL (2001): Analysis of partial volume effects in diffusion-tensor MRI. Magn Reson Med 45:770–780.

Andersson JL, Sotiropoulos SN (2016): An integrated approach to correction for off-resonance effects and subject movement in diffusion MR imaging. NeuroImage 125:1063–1078.

Apaydin H, Ahlskog JE, Parisi JE, Boeve BF, Dickson DW (2002): Parkinson disease neuropathology: Later-developing dementia and loss of the levodopa response. Arch Neurol 59:102–112.

Ashburner J (2007): A fast diffeomorphic image registration algorithm. NeuroImage 38:95–113.

Ashburner J, Friston KJ (2000): Voxel-based morphometry–the methods. NeuroImage 11:805–821.

Ashburner J, Friston KJ (2005): Unified segmentation. NeuroImage 26:839–851.

Ball G, Srinivasan L, Aljabar P, Counsell SJ, Durighel G, Hajnal JV, Rutherford MA, Edwards AD (2013): Development of cortical microstructure in the preterm human brain. Proc Natl Acad Sci U S A 110:9541–9546.

Bach M1, Laun FB1, Leemans A2, Tax CM2, Biessels GJ3, Stieltjes B4, Maier-Hein KH5 (2014): Methodological considerations on tract-based spatial statistics (TBSS). Neuroimage 100:358–369.

Basser PJ, Mattiello J, LeBihan D (1994): Estimation of the effective self-diffusion tensor from the NMR spin echo. Journal of magnetic resonance. Series B 103:247–254.

Basser PJ, Jones DK (2002): Diffusion-tensor MRI: Theory, experimental design and data analysis - a technical review. NMR Biomed 15:456–467.

Biundo R, Formento-Dojot P, Facchini S, Vallelunga A, Ghezzo L, Foscolo L, Meneghello F, Antonini A (2011): Brain volume changes in Parkinson's disease and their relationship with cognitive and behavioural abnormalities. J Neurol Sci 310:64–69.

Bonnet AM, Loria Y, Saint-Hilaire MH, Lhermitte F, Agid Y (1987): Does long-term aggravation of Parkinson's disease result from nondopaminergic lesions?. Neurology 37:1539–1542.

Braak H, Del Tredici K (2008): Invited Article: Nervous system pathology in sporadic Parkinson disease. Neurology 70: 1916–1925.

Braak H, Ghebremedhin E, Rub U, Bratzke H, Del Tredici K (2004): Stages in the development of Parkinson's disease-related pathology. Cell Tissue Res 318:121–134.

Braak H, Rub U, Jansen Steur EN, Del Tredici K, de Vos RA (2005): Cognitive status correlates with neuropathologic stage in Parkinson disease. Neurology 64:1404–1410.

Bruck A, Kurki T, Kaasinen V, Vahlberg T, Rinne JO (2004): Hippocampal and prefrontal atrophy in patients with early non-demented Parkinson's disease is related to cognitive impairment. J Neurol Neurosurg Psychiatry 75:1467–1469.

Burton EJ, McKeith IG, Burn DJ, Williams ED, O'Brien JT (2004): Cerebral atrophy in Parkinson's disease with and without dementia: A comparison with Alzheimer's disease, dementia with Lewy bodies and controls. Brain: J Neurol 127:791–800.

Cerasa A, Messina D, Pugliese P, Morelli M, Lanza P, Salsone M, Novellino F, Nicoletti G, Arabia G, Quattrone A (2011): Increased prefrontal volume in PD with levodopa-induced dyskinesias: A voxel-based morphometry study. Mov Disord 26:807–812.

Chan LL, Rumpel H, Yap K, Lee E, Loo HV, Ho GL, Fook-Chong S, Yuen Y, Tan EK (2007): Case control study of diffusion tensor imaging in Parkinson's disease. J Neurol Neurosurg Psychiatry 78:1383–1386.

Chesselet MF, Richter F, Zhu C, Magen I, Watson MB, Subramaniam SR (2012): A progressive mouse model of Parkinson's disease: The Thy1-aSyn ("Line 61") mice. Neurotherapeutics 9:297–314.

Claassen DO, McDonell KE, Donahue M, Rawal S, Wylie SA, Neimat JS, Kang H, Hedera P, Zald D, Landman B, Dawant B, Rane S (2016): Cortical asymmetry in Parkinson's disease: Early susceptibility of the left hemisphere. Brain Behav 6:e00573.

Cochrane CJ, Ebmeier KP (2013): Diffusion tensor imaging in parkinsonian syndromes: A systematic review and meta-analysis. Neurology 80:857–864.

Cohen J (1992): A power primer. Psychol Bull 112:155–159.

Daducci A, Canales-Rodriguez EJ, Zhang H, Dyrby TB, Alexander DC, Thiran JP (2015): Accelerated Microstructure Imaging via Convex Optimization (AMICO) from diffusion MRI data. NeuroImage 105:32–44.

Delenclos M, Carrascal L, Jensen K, Romero-Ramos M (2014): Immunolocalization of human alpha-synuclein in the Thy1-aSyn ("Line 61") transgenic mouse line. Neuroscience 277: 647–664.

Djaldetti R, Ziv I, Melamed E (2006): The mystery of motor asymmetry in Parkinson's disease. Lancet Neurol 5:796–802.

Falangola MF, Jensen JH, Babb JS, Hu C, Castellanos FX, Di Martino A, Ferris SH, Helpern JA (2008): Age-related non-Gaussian diffusion patterns in the prefrontal brain. J Magn Reson Imaging: JMRI 28:1345–1350.

Feldmann A, Illes Z, Kosztolanyi P, Illes E, Mike A, Kover F, Balas I, Kovacs N, Nagy F (2008): Morphometric changes of gray matter in Parkinson's disease with depression: A voxel-based morphometry study. Mov Disord 23:42–46.

Fieremans E, Jensen JH, Helpern JA (2011): White matter characterization with diffusional kurtosis imaging. NeuroImage 58: 177–188.

Fischl B, Dale AM (2000): Measuring the thickness of the human cerebral cortex from magnetic resonance images. Proc Natl Acad Sci U S A 97:11050–11055.

Fischl B, Sereno MI, Tootell RB, Dale AM (1999): High-resolution intersubject averaging and a coordinate system for the cortical surface. Hum Brain Mapp 8:272–284.

Focke NK, Helms G, Pantel PM, Scheewe S, Knauth M, Bachmann CG, Ebentheuer J, Dechent P, Paulus W, Trenkwalder C (2011): Differentiation of typical and atypical Parkinson syndromes by quantitative MR imaging. AJNR Am J Neuroradiol 32:2087–2092.

Gattellaro G, Minati L, Grisoli M, Mariani C, Carella F, Osio M, Ciceri E, Albanese A, Bruzzone MG (2009): White matter involvement in idiopathic Parkinson disease: A diffusion tensor imaging study. AJNR: Am J Neuroradiol 30:1222–1226.

Greffard S, Verny M, Bonnet AM, Beinis JY, Gallinari C, Meaume S, Piette F, Hauw JJ, Duyckaerts C (2006): Motor score of the Unified Parkinson Disease Rating Scale as a good predictor of Lewy body-associated neuronal loss in the substantia nigra. Arch Neurol 63:584-8.

Herman T, Weiss A, Brozgol M, Giladi N, Hausdorff JM (2014): Gait and balance in Parkinson's disease subtypes: Objective measures and classification considerations. J Neurol 261:2401–2410.

Hoehn MM, Yahr MD (1967): Parkinsonism: Onset, progression and mortality. Neurology 17:427–442.

Hughes AJ, Daniel SE, Kilford L, Lees AJ (1992): Accuracy of clinical diagnosis of idiopathic Parkinson's disease: A clinico-pathological study of 100 cases. J Neurol Neurosurg Psychiatry 55:181–184.

Jellinger KA (2012): Neuropathology of sporadic Parkinson's disease: Evaluation and changes of concepts. Mov Disord 27:8–30.

Jenkinson M, Bannister P, Brady M, Smith S (2002): Improved optimization for the robust and accurate linear registration and motion correction of brain images. NeuroImage 17:825–841.

Jenkinson M, Beckmann CF, Behrens TE, Woolrich MW, Smith SM (2012): Fsl. NeuroImage 62:782–790.

Jensen JH, Helpern JA (2010): MRI quantification of non-Gaussian water diffusion by kurtosis analysis. NMR Biomed 23:698–710.

Jensen JH, Helpern JA, Ramani A, Lu H, Kaczynski K (2005): Diffusional kurtosis imaging: The quantification of non-gaussian water diffusion by means of magnetic resonance imaging. Magn Reson Med 53:1432–1440.

Johansen-Berg H, Behrens TEJ (2014): Diffusion MRI: From Quantitative Measurement to In-Vivo Neuroanatomy. London, UK; Waltham, MA: Elsevier/Academic Press.

Jubault T, Gagnon JF, Karama S, Ptito A, Lafontaine AL, Evans AC, Monchi O (2011): Patterns of cortical thickness and surface area in early Parkinson's disease. NeuroImage 55:462–467.

Kamagata K, Motoi Y, Abe O, Shimoji K, Hori M, Nakanishi A, Sano T, Kuwatsuru R, Aoki S, Hattori N (2012): White matter

alteration of the cingulum in Parkinson disease with and without dementia: Evaluation by diffusion tensor tract-specific analysis. AJNR Am J Neuroradiol 33:890.

Kamagata K, Motoi Y, Tomiyama H, Abe O, Ito K, Shimoji K, Suzuki M, Hori M, Nakanishi A, Sano T, Kuwatsuru R, Sasai K, Aoki S, Hattori N (2013): Relationship between cognitive impairment and white-matter alteration in Parkinson's disease with dementia: Tract-based spatial statistics and tract-specific analysis. Eur Radiol 23:1946–1955.

Kamagata K, Hatano T, Okuzumi A, Motoi Y, Abe O, Shimoji K, Kamiya K, Suzuki M, Hori M, Kumamaru KK, Hattori N, Aoki S (2015): Neurite orientation dispersion and density imaging in the substantia nigra in idiopathic Parkinson disease. Eur Radiol 26:2567–2577.

Karagulle Kendi AT, Lehericy S, Luciana M, Ugurbil K, Tuite P (2008): Altered diffusion in the frontal lobe in Parkinson disease. AJNR Am J Neuroradiol 29:501–505.

Kempster PA, Gibb WR, Stern GM, Lees AJ (1989): Asymmetry of substantia nigra neuronal loss in Parkinson's disease and its relevance to the mechanism of levodopa related motor fluctuations. J Neurol Neurosurg Psychiatry 52:72–76.

Khairnar A, Latta P, Drazanova E, Ruda-Kucerova J, Szabo N, Arab A, Hutter-Paier B, Havas D, Windisch M, Sulcova A, Starcuk Z, Jr, Rektorova I (2015a): Diffusion kurtosis imaging detects microstructural alterations in brain of alpha-synuclein overexpressing transgenic mouse model of parkinson's disease: A pilot study. Neurotoxic Res 28:281–289.

Khairnar A, Ruda-Kucerova J, Drazanova E, Szabo N, Latta P, Arab A, Hutter-Paier B, Havas D, Windisch M, Sulcova A, Starcuk Z, Jr., Kiraly A, Rektorova I (2015b): Late-stage alpha-synuclein accumulation in TNWT-61 mouse model of Parkinson's disease detected by diffusion kurtosis imaging. J Neurochem 136:1259–1269.

Koch JC, Bitow F, Haack J, d'Hedouville Z, Zhang JN, Tonges L, Michel U, Oliveira LM, Jovin TM, Liman J, Tatenhorst L, Bahr M, Lingor P (2015): Alpha-Synuclein affects neurite morphology, autophagy, vesicle transport and axonal degeneration in CNS neurons. Cell Death Dis 6:e1811.

Lee JE, Chung MK, Lazar M, DuBray MB, Kim J, Bigler ED, Lainhart JE, Alexander AL (2009): A study of diffusion tensor imaging by tissue-specific, smoothing-compensated voxel-based analysis. NeuroImage 44:870–883.

Lu H, Jensen JH, Ramani A, Helpern JA (2006): Three-dimensional characterization of non-gaussian water diffusion in humans using diffusion kurtosis imaging. NMR Biomed 19:236–247.

Lyoo CH, Ryu YH, Lee MS (2010): Topographical distribution of cerebral cortical thinning in patients with mild Parkinson's disease without dementia. Mov Disord 25:496–499.

Mak E, Su L, Williams GB, Firbank MJ, Lawson RA, Yarnall AJ, Duncan GW, Owen AM, Khoo TK, Brooks DJ, Rowe JB, Barker RA, Burn DJ, O'Brien JT (2015): Baseline and longitudinal grey matter changes in newly diagnosed Parkinson's disease: ICICLE-PD study. Brain: J Neurol 138:2974–2986.

Martinez-Martin P, Gil-Nagel A, Gracia LM, Gomez JB, Martinez-Sarries J, Bermejo F (1994): Unified Parkinson's Disease Rating Scale characteristics and structure. The Cooperative Multicentric Group. Mov Disord 9:76–83.

Menke RA, Scholz J, Miller KL, Deoni S, Jbabdi S, Matthews PM, Zarei M (2009): MRI characteristics of the substantia nigra in Parkinson's disease: A combined quantitative T1 and DTI study. NeuroImage 47:435–441.

Meppelink AM, de Jong BM, Teune LK, van Laar T (2011): Regional cortical grey matter loss in Parkinson's disease without dementia is independent from visual hallucinations. Mov Disord 26:142–147.

Messina D, Cerasa A, Condino F, Arabia G, Novellino F, Nicoletti G, Salsone M, Morelli M, Lanza PL, Quattrone A (2011): Patterns of brain atrophy in Parkinson's disease, progressive supranuclear palsy and multiple system atrophy. Parkinsonism Relat Disord 17:172–176.

Morfini GA, Burns M, Binder LI, Kanaan NM, LaPointe N, Bosco DA, Brown RH, Jr., Brown H, Tiwari A, Hayward L, Edgar J, Nave KA, Garberrn J, Atagi Y, Song Y, Pigino G, Brady ST (2009): Axonal transport defects in neurodegenerative diseases. J Neurosci 29:12776–12786.

Nazeri A, Chakravarty MM, Rotenberg DJ, Rajji TK, Rathi Y, Michailovich OV, Voineskos AN (2015): Functional consequences of neurite orientation dispersion and density in humans across the adult lifespan. J Neurosci 35:1753–1762.

Nicoletti G, Rizzo G, Barbagallo G, Tonon C, Condino F, Manners D, Messina D, Testa C, Arabia G, Gambardella A, Lodi R, Quattrone A (2013): Diffusivity of cerebellar hemispheres enables discrimination of cerebellar or parkinsonian multiple system atrophy from progressive supranuclear palsy-Richardson syndrome and Parkinson disease. Radiology 267:843–850.

Paviour DC, Price SL, Jahanshahi M, Lees AJ, Fox NC (2006): Longitudinal MRI in progressive supranuclear palsy and multiple system atrophy: Rates and regions of atrophy. Brain: J Neurol 129:1040–1049.

Perlson E, Maday S, Fu MM, Moughamian AJ, Holzbaur EL (2010): Retrograde axonal transport: Pathways to cell death?. Trends Neurosci 33:335–344.

Prakash BD, Sitoh YY, Tan LC, Au WL (2012): Asymmetrical diffusion tensor imaging indices of the rostral substantia nigra in Parkinson's disease. Parkinsonism Relat Disord 18:1029–1033.

Rizzo G, Martinelli P, Manners D, Scaglione C, Tonon C, Cortelli P, Malucelli E, Capellari S, Testa C, Parchi P, Montagna P, Barbiroli B, Lodi R (2008): Diffusion-weighted brain imaging study of patients with clinical diagnosis of corticobasal degeneration, progressive supranuclear palsy and Parkinson's disease. Brain: J Neurol 131:2690–2700.

Rose SE, Janke AL, Chalk JB (2008): Gray and white matter changes in Alzheimer's disease: A diffusion tensor imaging study. J Magn Reson Imaging: JMRI 27:20–26.

Scherfler C, Seppi K, Mair KJ, Donnemiller E, Virgolini I, Wenning GK, Poewe W (2012): Left hemispheric predominance of nigrostriatal dysfunction in Parkinson's disease. Brain: J Neurol 135:3348–3354.

Schwarz CG, Reid RI, Gunter JL, Senjem ML, Przybelski SA, Zuk SM, Whitwell JL, Vemuri P, Josephs KA, Kantarci K, Thompson PM, Petersen RC, Jack CR, Jr; Alzheimer's Disease Neuroimaging Initiative (2014): Improved DTI registration allows voxel-based analysis that outperforms tract-based spatial statistics. Neuroimage 94:65–78.

Seppi K, Poewe W (2010): Brain magnetic resonance imaging techniques in the diagnosis of parkinsonian syndromes. Neuroimaging Clin N Am 20:29–55.

Smith SM (2002): Fast robust automated brain extraction. Hum Brain Mapp 17:143–155.

Smith SM, Nichols TE (2009): Threshold-free cluster enhancement: Addressing problems of smoothing, threshold dependence and localisation in cluster inference. NeuroImage 44:83–98.

Smith SM, Jenkinson M, Johansen-Berg H, Rueckert D, Nichols TE, Mackay CE, Watkins KE, Ciccarelli O, Cader MZ, Matthews PM, Behrens TE (2006): Tract-based spatial statistics: Voxelwise analysis of multi-subject diffusion data. NeuroImage 31:1487–1505.

Surova Y, Lampinen B, Nilsson M, Latt J, Hall S, Widner H, Swedish Bio Fs, van Westen D, Hansson O (2016): Alterations of diffusion kurtosis and neurite density measures in deep grey matter and white matter in Parkinson's disease. PLoS One 11:e0157755.

Tabesh A, Jensen JH, Ardekani BA, Helpern JA (2011): Estimation of tensors and tensor-derived measures in diffusional kurtosis imaging. Magn Reson Med 65:823–836.

Tinaz S, Courtney MG, Stern CE (2011): Focal cortical and subcortical atrophy in early Parkinson's disease. Mov Disord 26: 436–441.

Vaillancourt DE, Spraker MB, Prodoehl J, Abraham I, Corcos DM, Zhou XJ, Comella CL, Little DM (2009): High-resolution diffusion tensor imaging in the substantia nigra of de novo Parkinson disease. Neurology 72:1378–1384.

Varoquaux G, Raamana PR, Engemann DA, Hoyos-Idrobo A, Schwartz Y, Thirion B (2017): Assessing and tuning brain decoders: Cross-validation, caveats, and guidelines. NeuroImage 145:166–179.

Veraart J, Poot DH, Van Hecke W, Blockx I, Van der Linden A, Verhoye M, Sijbers J (2011): More accurate estimation of diffusion tensor parameters using diffusion Kurtosis imaging. Magn Reson Med 65:138–145.

Von Coelln R, Shulman LM (2016): Clinical subtypes and genetic heterogeneity: Of lumping and splitting in Parkinson disease. Curr Opin Neurol 29:727–734.

Wang JJ, Lin WY, Lu CS, Weng YH, Ng SH, Wang CH, Liu HL, Hsieh RH, Wan YL, Wai YY (2011): Parkinson disease: Diagnostic utility of diffusion kurtosis imaging. Radiology 261: 210–217.

Winkler AM, Ridgway GR, Webster MA, Smith SM, Nichols TE (2014): Permutation inference for the general linear model. NeuroImage 92:381–397.

Yang AW, Jensen JH, Hu CC, Tabesh A, Falangola MF, Helpern JA (2013): Effect of cerebral spinal fluid suppression for diffusional kurtosis imaging. J Magn Reson Imaging: JMRI 37: 365–371.

Yoshikawa K, Nakata Y, Yamada K, Nakagawa M (2004): Early pathological changes in the parkinsonian brain demonstrated by diffusion tensor MRI. J Neurol Neurosurg Psychiatry 75: 481–484.

Zalesky A (2011): Moderating registration misalignment in voxelwise comparisons of DTI data: a performance evaluation of skeleton projection. Magn Reson Imaging. 29:111–125.

Zhan W, Kang GA, Glass GA, Zhang Y, Shirley C, Millin R, Possin KL, Nezamzadeh M, Weiner MW, Marks WJ, Jr, Schuff N (2012): Regional alterations of brain microstructure in Parkinson's disease using diffusion tensor imaging. Mov Disord 27:90–97.

Zhang Y, Brady M, Smith S (2001): Segmentation of brain MR images through a hidden Markov random field model and the expectation-maximization algorithm. IEEE Trans Med Imaging 20:45–57.

Zhang H, Schneider T, Wheeler-Kingshott CA, Alexander DC (2012): NODDI: Practical in vivo neurite orientation dispersion and density imaging of the human brain. NeuroImage 61:1000–1016.